

Conformal Disentanglement: A Neural Framework for Perspective Synthesis and Differentiation

George A. Kevrekidis^{1,3}, Eleni D. Koronaki², and Yannis G. Kevrekidis¹

¹*Department of Applied Mathematics and Statistics, Johns Hopkins University, Baltimore, MD, USA*

²*Faculty of Science, Technology and Medicine, University of Luxembourg, Esch-sur-Alzette, Luxembourg*

³*Los Alamos National Laboratory, Los Alamos, NM, USA*

August 27, 2024
LA-UR-24-28862

Abstract

For multiple scientific endeavors it is common to measure a phenomenon of interest in more than one ways. We make observations of objects from several different perspectives in space, at different points in time; we may also measure different properties of a mixture using different types of instruments. After collecting this heterogeneous information, it is necessary to be able to synthesize a complete picture of what is ‘common’ across its sources: the subject we ultimately want to study. However, isolated (‘clean’) observations of a system are not always possible: observations often contain information about other systems in its environment, or about the measuring instruments themselves. In that sense, each observation may contain information that ‘does not matter’ to the original object of study; this ‘uncommon’ information between sensors observing the same object may still be important, and decoupling it from the main signal(s) useful. We introduce a neural network autoencoder framework capable of *both* tasks: it is structured to identify ‘common’ variables, and, making use of orthogonality constraints to define geometric independence, to also identify disentangled ‘uncommon’ information originating from the heterogeneous sensors. We demonstrate applications in several computational examples.

1 Introduction

Perspective Synthesis and Perspective Differentiation [1] encompass a collection of computational inference tasks that arise when a system of interest is observed by multiple, possibly multi-modal observers. We will jointly, and more colloquially, refer to them as the ‘Common & Uncommon Variable’ problem.

An intuitive example was introduced in [2, 3], which we paraphrase as follows:

Example 1. We have three people (Alice, Bob, and Carol) standing (not idly!) in a line, and two cameras recording their motion, such that Camera 1 sees Alice and Bob, and Camera 2 sees Bob and Carol, over a long period of time (Fig. 1). While both cameras see Bob, it is from a different angle, and they do not capture the same perspective at any given time. Given sequences of snapshots recorded over a long period of time simultaneously from both cameras, we would like to be able to identify that Bob is actually *the same person*, just seen from different perspectives, while Alice and Carol are *different* persons; and, given Bob’s observation by one of the cameras, infer his observation at the same time instance by the other camera. That is (even though it is colloquially awkward), in Systems parlance, we want to build an observer of camera 2 observations from camera 1 observations.

More generally, *Perspective Synthesis*, or the ‘Common Variable’ problem, addresses the identification of the part of data that is *common* between several observers. Subsequently, *Perspective Differentiation*, or the ‘Uncommon Variable’ problem, refers to separating the part of the observed data that is *unique* to each instrument. This separation is only possible *after* the common part has been identified, and is also commonly referred to as ‘disentanglement’.

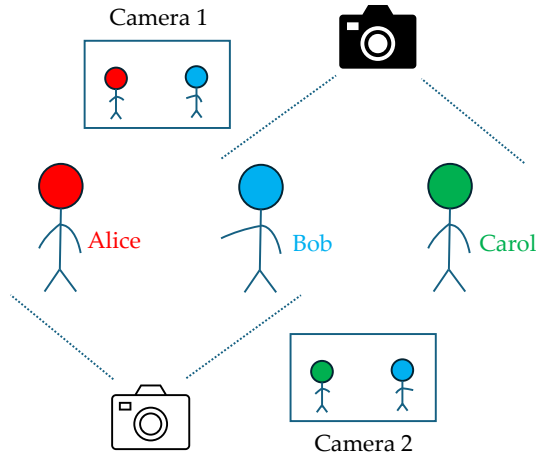


Figure 1: Caricature described in Example 1. Bob (blue, middle) is observed from different perspectives by two cameras. Alice (red, left) is only observed by camera 1, and Carol (green, right) is only observed by camera 2.

In this work, we propose a neural network architecture capable of simultaneously tackling both problems. Our approach follows a geometric perspective, as formalized in Section 2.

Literature

The numerical tasks we discuss have previously been achieved (to some extent) with variants of the classical Diffusion Map algorithm [4] and, more generally, kernel-based spectral methods commonly used for dimension reduction. More specifically, the Alternating Diffusion algorithm [2, 3] was proposed for the identification of the Common variables in a similar multi-observer setting. Identification of the Uncommon parts between two data sets has been initially discussed in [5], based on an idea originally presented in S. Lafon’s dissertation [6], referred to as the ‘Output-Informed’ Diffusion Map algorithm. It has also been achieved spectrally in [7] as a variant on the ‘Jointly Smooth Functions’ algorithm. A related approach is presented in [8]. Studies of Canonical Correlation Analysis [9], Nonlinear Independent Component Analysis [10], and Contrastive Learning [11] are also connected to the subject.

It is useful to discriminate between two cases: In the first, at the input level (consistent with the caricature in Fig. 1), each camera pixel is only associated with one of the two observed systems (either the common or the uncommon one): Topics in contact Hamiltonian systems Bob and Alice do not overlap, and neither do Bob and Carol. We call this the ‘clean’ pixel case. Our methodology is more general, in that it allows us to deal with systems for which, at the input level, pixels are jointly influenced by *both* observed systems (e.g. Alice *and* Bob); we call this the ‘dirty pixel’ case. As we will see below, the ‘dirty’ pixels case creates interesting challenges for what observations of one camera can say about observations of the other. Other algorithms in the cited literature are also capable of dealing with this more general framework.

Structure and Contributions

In Section 2 we outline a formal mathematical setting to describe the Common & Uncommon variable problem through a differential-geometric lens. In Section 3 we describe the proposed architecture and optimization algorithm, before demonstrating its application on several computational examples in Section 4. In Section 5 we briefly discuss the special situation where camera 1 observes snapshots of an evolving dynamical system, while camera 2 observes the same system in the future, i.e. featuring a constant time shift (similar to the setting of the classical Takens embedding theorem [12]). We discuss and conclude in Section 6.

Main Contributions:

- ◆ We propose and implement a structured autoencoder architecture capable of **identifying ‘common’** variables and **disentangling** from them **‘uncommon’** variables for observations of multiple systems made by two sensors. This can be easily generalized to the case of multiple sensors.
- ◆ We propose the use of (block-) **orthogonality** constraints to *define geometric independence*.
- ◆ We demonstrate applicability of the framework in a dynamical system context, both for synthetic data and for high-dimensional image data.
- ◆ In studying relations across sensors, we discover and parametrize **level sets** of one sensor’s observations consistent with a single observation of the other sensor.

2 Problem Statement

Mnemonically, we will use the upper- and lower-case letter ‘C’ to label concepts related to the ‘common’ system, and the upper- and lower-case letters ‘U’ and ‘V’ for concepts related to each of the ‘uncommon’ systems. We describe the setting for two sensors observing a total of three systems, one of which is common; it is straightforward to extend to different settings with multiple sensors (involving arbitrary, possibly intricate choices of what is common and uncommon between different subsets of sensors).

Setup: We let

$$\begin{aligned} \mathcal{U} &\hookrightarrow \mathbb{R}^{n_u}, & \dim \mathcal{U} &= d_u \\ \mathcal{V} &\hookrightarrow \mathbb{R}^{n_v}, & \dim \mathcal{V} &= d_v \\ \mathcal{C} &\hookrightarrow \mathbb{R}^{n_c}, & \dim \mathcal{C} &= d_c \end{aligned} \tag{1}$$

be three embedded submanifolds of Euclidean space where, in each case, the ambient (n_u, n_v, n_c) and intrinsic (d_u, d_v, d_c) dimensions are known. Here, $\mathcal{C}, \mathcal{U}, \mathcal{V}$ represent the common and two uncommon systems respectively. For each submanifold, it is possible for the ambient and intrinsic dimensions to be equal, but they generically are not; In the case where the common system \mathcal{C} is a circle, for example, we would have $n_c = 2$ and $d_c = 1$. We will assume that all $n_u, n_v, n_c, d_u, d_v, d_c$ are known, and that the embedding Euclidean dimensions n_u, n_v, n_c are minimal for smooth embeddings to exist [13].

Suppose that we are given two sets S_1, S_2 of sampled snapshots as data from the two sensors:

$$\begin{aligned} S_1 &= \{s_{u,i} \in \mathbb{R}^{k_u}\}_{i=1}^N \\ S_2 &= \{s_{v,i} \in \mathbb{R}^{k_v}\}_{i=1}^N \end{aligned} \tag{2}$$

where the observed data dimensions k_u and k_v are possibly large. In particular, these will satisfy the following inequalities such that there is no information lost:

$$\begin{aligned} k_u &\geq n_u + n_c \\ k_v &\geq n_v + n_c \end{aligned} \tag{3}$$

though an additional dimension reduction step can convert the problem to one where equality holds in Eqn. (3).

Furthermore, we assume that there exist two smooth, left-invertible maps (Φ_u, Φ_v) such that

$$\begin{aligned}\Phi_u(S_1) = D_u &= \{\mathbf{d}_{1,i} \in \mathcal{U} \times \mathcal{C}\}_{i=1}^N \subset \mathbb{R}^{n_u+n_c} \\ \Phi_v(S_2) = D_v &= \{\mathbf{d}_{2,i} \in \mathcal{V} \times \mathcal{C}\}_{i=1}^N \subset \mathbb{R}^{n_v+n_c}\end{aligned}\tag{4}$$

where individual snapshots can be written in their coordinate form

$$\begin{aligned}\mathbf{d}_1 &= (u_1, \dots, u_{n_u}, c_1, \dots, c_{n_c}) \\ \mathbf{d}_2 &= (v_1, \dots, v_{n_v}, c'_1, \dots, c'_{n_c})\end{aligned}\tag{5}$$

which are coordinates of the respective Euclidean embedding spaces, restricted to the (non-linear) submanifolds. That is to say, even though the observations may be possibly high-dimensional (k_u, k_v) , the data lie on lower-dimensional submanifolds in Euclidean space, and furthermore these **are ‘factorizable’ into a product of two ‘disentangled’ submanifolds, respectively, for each sensor.**

After applying Φ_u, Φ_v , we can define the natural projections $\pi_u, \pi_v, \pi_c, \pi_{c'}$ on the corresponding coordinates of the three disentangled submanifolds. We will additionally assume that there exists a diffeomorphism φ on the common submanifold:

$$\varphi : \mathcal{C} \rightarrow \mathcal{C} \text{ such that } \varphi \circ \pi_c(\mathbf{d}_{1,i}) = \pi_{c'}(\mathbf{d}_{2,i})\tag{6}$$

which establishes pointwise correspondence, meaning that the \mathcal{C} appearing in the two data sets is ‘the same object’. Thus, S_1, S_2 can be shuffled by a permutation in their indices, as long as it is the same permutation across both data sets. The pair-correspondence *between simultaneous snapshots* is what determines the common submanifold uniquely up to the diffeomorphism φ .

Interpretation: The setup generalizes the task described in the introduction: two sensors (S_1, S_2) make simultaneous observations, parts of which are (different) observations of the same ‘common’ system. This is abstractly represented by the common submanifold \mathcal{C} . However, the common observations need not be identical, as long as they are equivalent up to a diffeomorphism φ (similar to having two cameras observe the same person from different perspectives). Each sensor, additionally, also observes some amount of ‘uncommon’ information which is ‘irrelevant’ with respect to \mathcal{C} , represented respectively as the uncommon submanifolds \mathcal{U} and \mathcal{V} . It is therefore reasonable to ask whether, given only sensor data in the form of Eqn. (2), we can recover ‘intrinsic’ parametrizations of *both* the common and the two uncommon systems.

Objective: Given samples of the form of Eqn. (2), we would like to: **(a)** Identify and parametrize the ‘common’ submanifold \mathcal{C} ; **(b)** Identify and parametrize each uncommon submanifold \mathcal{U}, \mathcal{V} . For now, we assume that topological and geometric characteristics of each submanifold are unknown, and we want to learn a representation of each submanifold as embedded individually in Euclidean space (Eqn. (1)).

Ultimately, we also want to **c.** establish relations between observations of one sensor and (level sets of) consistent observations of the other sensor.

3 Methods

In this section we outline an approach to solving the problem described in Section 2 using bespoke autoencoder neural networks. Specifically, we develop an architecture and implement appropriate optimization algorithms, which are suitable for recovering the desired parametrizations of the common and uncommon submanifolds.

3.1 Network Architectures

We define encoder-decoder pairs separately for each data set. Each encoder consists of common and uncommon parts as follows (see also Fig. 2):

For S_1 :

- The encoder $\epsilon_1 : \mathbb{R}^{k_u} \rightarrow \mathbb{R}^{d_u+d_c}$ consists of two maps aimed at separating the common and uncommon parts:

$$\epsilon_1^c : \mathbb{R}^{k_u} \rightarrow \mathbb{R}^{d_c}, \quad \mathbf{s}_u \mapsto \hat{\mathbf{c}}_u \quad (\text{common}) \quad (7)$$

$$\epsilon_1^u : \mathbb{R}^{k_u} \rightarrow \mathbb{R}^{d_u}, \quad \mathbf{s}_u \mapsto \hat{\mathbf{u}} \quad (\text{uncommon 1}) \quad (8)$$

- The decoder $\mathfrak{d}_1 : \mathbb{R}^{d_u+d_c} \rightarrow \mathbb{R}^{k_u}, (\hat{\mathbf{c}}_u, \hat{\mathbf{u}}) \mapsto \hat{\mathbf{s}}_u$ consists of a single map intended to approximate the left inverse of the entire encoder ϵ_1 .

Similarly, for S_2 :

- The encoder $\epsilon_2 : \mathbb{R}^{k_v} \rightarrow \mathbb{R}^{d_u+d_c}$ consists of two maps aimed at separating the common and uncommon parts:

$$\epsilon_2^c : \mathbb{R}^{k_v} \rightarrow \mathbb{R}^{d_c}, \quad \mathbf{s}_v \mapsto \hat{\mathbf{c}}_v \quad (\text{common}) \quad (9)$$

$$\epsilon_2^u : \mathbb{R}^{k_v} \rightarrow \mathbb{R}^{d_u}, \quad \mathbf{s}_v \mapsto \hat{\mathbf{v}} \quad (\text{uncommon 2}) \quad (10)$$

- The decoder $\mathfrak{d}_2 : \mathbb{R}^{d_u+d_c} \rightarrow \mathbb{R}^{k_v}, (\hat{\mathbf{c}}_v, \hat{\mathbf{v}}) \mapsto \hat{\mathbf{s}}_v$ consists of a single map intended to approximate the left inverse of the entire encoder ϵ_2 .

A diagram of the proposed architecture is presented in Fig. 2. In practice, each map is parametrized by a single fully connected multilayer neural network with smooth activations.

3.2 Bi-Level Optimization Algorithm

The goal of our optimization task is to approximate the maps Φ_u, Φ_v and the embedding coordinates of Eqn. (5), up to diffeomorphisms. Upon successful training of the architecture parameters, the decoder outputs will be ‘good’ reconstructions of the input data, i.e. each combined encoder (ϵ_1, ϵ_2) has a left inverse that is well-approximated by each of the decoders ($\mathfrak{d}_1, \mathfrak{d}_2$) in some appropriate norm (usually specified to be ℓ^2 (MSE) for individual points in the training data set).

There is a total of three objectives we aim to simultaneously satisfy:

$$\mathcal{L}_{\text{reconstruction}} = \frac{1}{N} \sum_{i=1}^N \left(\|\mathbf{s}_{u,i} - \hat{\mathbf{s}}_{u,i}\|_2^2 + \|\mathbf{s}_{v,i} - \hat{\mathbf{s}}_{v,i}\|_2^2 \right) \quad (11)$$

$$\mathcal{L}_{\text{common}} = \frac{1}{N} \sum_{i=1}^N \|\hat{\mathbf{c}}_{u,i} - \hat{\mathbf{c}}_{v,i}\|_2^2 \quad (12)$$

$$\mathcal{L}_{\text{orthogonality}} = \frac{1}{N} \sum_{i=1}^N \left(\sum_{j,k} \langle \nabla(\epsilon_1^u(\mathbf{s}_{u,i}))_j, \nabla(\epsilon_1^c(\mathbf{s}_{u,i}))_k \rangle + \sum_{l,k} \langle \nabla(\epsilon_2^u(\mathbf{s}_{v,i}))_k, \nabla(\epsilon_2^c(\mathbf{s}_{v,i}))_l \rangle \right) \quad (13)$$

Individually, minimizing $\mathcal{L}_{\text{reconstruction}}$ ensures that each encoder is left-invertible, while minimizing $\mathcal{L}_{\text{common}}$ biases the common encoders ($\epsilon_1^c, \epsilon_2^c$) to find the same common latent embedding. Finally, $\mathcal{L}_{\text{orthogonality}}$ is a measure of (block-) functional independence, forcing the gradients of the functions parametrizing the uncommon systems within a sensor to be pointwise perpendicular to those parametrizing the common. Here, the indices j, l range over n_u, n_v respectively, while the index k ranges over n_c . The inner product is inherited by the Euclidean ambient space in which the input data is represented.

We propose the following bi-level optimization procedure:

Step 1. Optimizing all encoder and decoder weights, we train the combined neural network architecture to identify the ‘common’ subspace of the data by minimizing

$$\mathcal{L}_1 = \mathcal{L}_{\text{reconstruction}} + \mathcal{L}_{\text{common}} \quad (14)$$

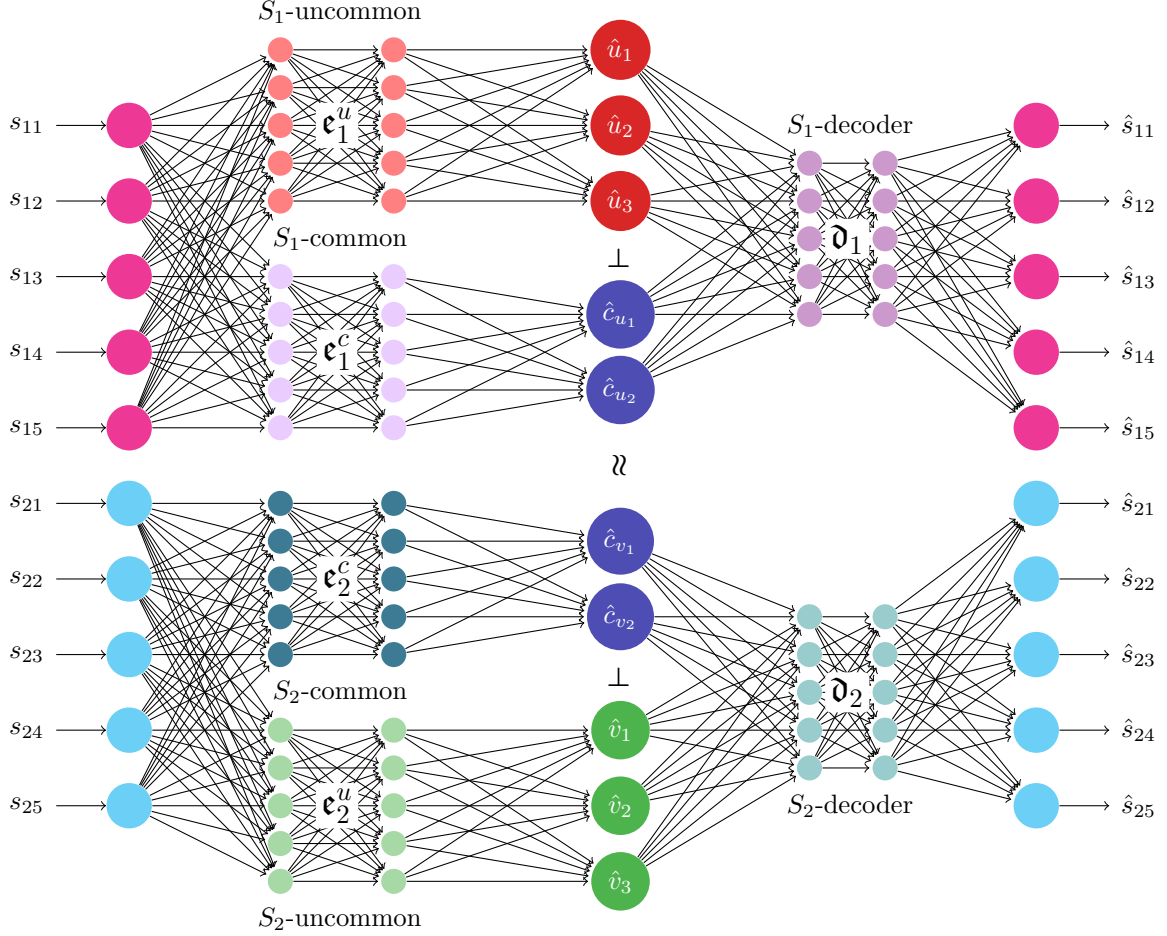


Figure 2: Sketch of the proposed network architecture outlined in Section 3.1. The dimensions of the input, output and latent spaces correspond to those of Example 3, while the encoder and decoder networks are just representations (and may have arbitrary width and depth)

Step 2. After fixing the common encoder weights ($\mathbf{e}_1^c, \mathbf{e}_2^c$), we add the orthogonality constraint between them and their respective uncommon maps ($\mathbf{e}_1^u, \mathbf{e}_2^u$), to now *disentangle* the uncommon component from the latent data representation. That is, we minimize:

$$\mathcal{L}_2 = \mathcal{L}_{\text{reconstruction}} + \mathcal{L}_{\text{orthogonality}} \quad (15)$$

A detailed description of the proposed algorithm is presented in Appendix B. Intentionally separating the weights of the common encoder component and uncommon encoder component for each system (as shown in Fig. 2) facilitates the process, in our experience, by allowing us to fix the common component weights *after* identifying the common subspace in step 1.

While, in principle, the proposed objectives do not compete, and can all three be minimized simultaneously, we have empirically observed that process to be less stable. Furthermore, minimizing $\mathcal{L}_{\text{orthogonality}}$ is only sensible *after* the common variables have been (at least approximately) identified; otherwise it is possible for this objective to initially steer the optimization to a ‘bad’ local minimum.

Finally, we note that minimizing the inner products of $\mathcal{L}_{\text{orthogonality}}$ is an attempt to *block-diagonalize the metric tensor* of the systems observed by each individual sensor, in the space where the observation occurs.

The common and uncommon systems are represented by their own blocks, and we penalize the ℓ^2 norm of the off-block-diagonal entries, at each point where we have an observation. This form of disentanglement is **differential and local**, in contrast to **statistical versions** which measure conditional dependence between variables (e.g. nonlinear Independent Component Analysis [10] or β -Variational Autoencoders [14]). Fundamentally what we achieve (for each sensor) is a latent parametrization which is a cross-product of two submanifolds. The effect of the orthogonality constraint is, we believe, clearly illustrated in Fig. 3.

We demonstrate the capabilities of the proposed architecture and algorithm in the examples that follow.

4 Computational Examples

We first study two synthetic examples arising in a dynamical systems context, before revisiting the ‘bobblehead problem’ introduced in [2], which resembles Example 1. The latter is a dynamical system in disguise but, nevertheless, showcases the ability of our architecture to identify common/uncommon underlying structures, that can be further used to generate high-dimensional images. Finally, we discuss an example where the two sets of observations are separated by a consistent time shift. This allows us to effectively learn a time-stepping map for an evolving system.

For additional details regarding the data generation, see Appendix A.

Example 2 (Torus). The data sets for this first computational example consist of samples of oscillator trajectories. These are combined using a random matrix, so that each observation contains information from both the common and uncommon systems. Each $\mathcal{U}, \mathcal{V}, \mathcal{C}$ are closed orbits (limit cycle-type trajectories). Both common and uncommon latent spaces are two-dimensional. Note that this is a minimal realization of the rotating bobblehead example in [2]. In Fig. 3 we visualize the resulting embedding of the data after the first (top row) and after the second (bottom row) levels of our optimization are completed. In the top row we see that the common subspaces (blue) are ‘correctly’ identified to be topological circles, while the uncommon ones (red and green) are random projections of the overall higher-dimensional (toroidal) data. After imposing the orthogonality constraints between the common and uncommon subspaces for each system, we recover the ‘decoupled’ circles in both cases. Each image is colored by the corresponding intrinsic variable θ_i (corresponding to the ‘correct’ coordinates on each subspace, up to diffeomorphism); these known *a priori* since the data set was generated synthetically, and should therefore vary smoothly upon proper convergence of the algorithm.

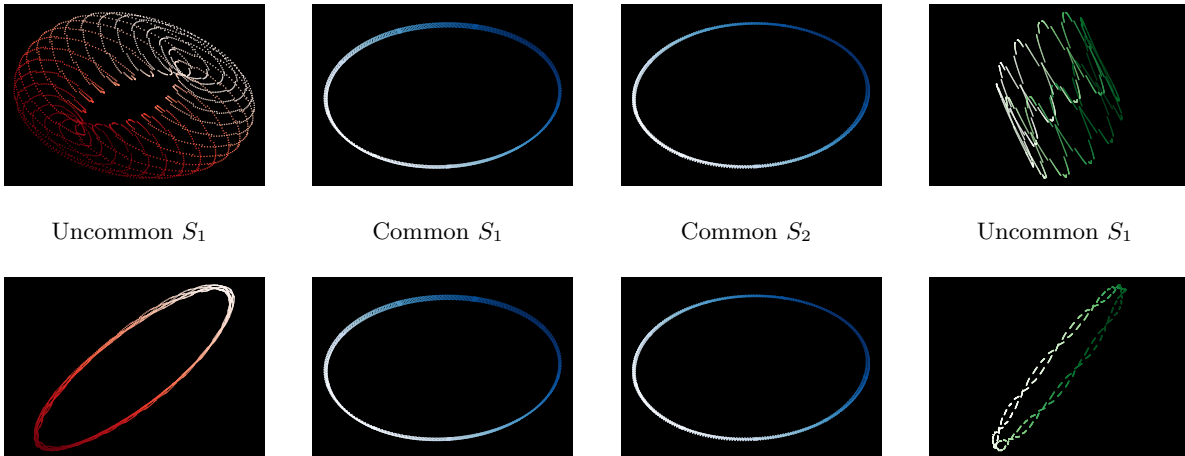


Figure 3: Latent embeddings produced for a single run of the optimization algorithm applied to Example 2. **(Top Row)** Result after successfully terminating the first level optimization (no orthogonality between the common and uncommon components). **(Bottom Row)** Resulting embedding after the second level of optimization (with orthogonality imposed).

To produce the corresponding figures, we use 54% of the data set for training, 36% for validation and 10% for testing. We terminate the first optimization step with training and validation losses of $1.1e-5$, $1.0e-5$ respectively, and the second optimization step with losses of $5.0e-4$, $9.1e-5$ respectively. The final test loss reported was $1.0e-4$.

Example 3 (Rössler & Lorenz Equations). The data sets for this second example consist again of samples of dynamical system trajectories, where \mathcal{U} is a Rössler attractor, \mathcal{V} is a Lorenz attractor, and \mathcal{C} is a (common) limit cycle. Once again, these are combined using a random matrix, so that each observation contains information from both the common and uncommon systems. Thus, the common subspace is two-dimensional while the uncommon ones are three-dimensional respectively. Once again, the recovered embeddings of Fig. 4 demonstrate the expected topological and geometric characteristics.

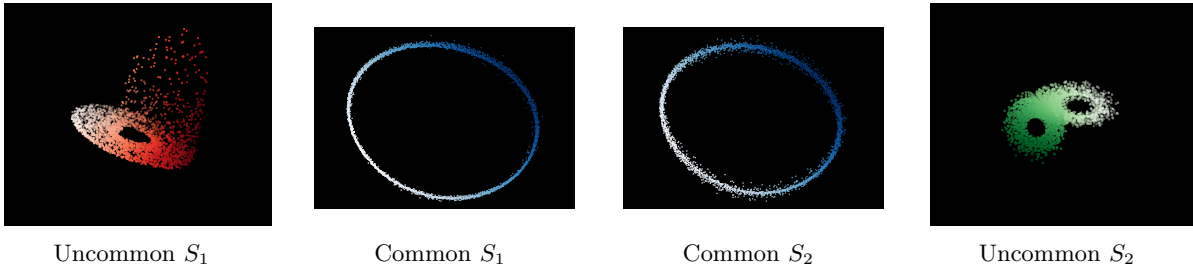


Figure 4: Latent embeddings produced for a single run of the optimization algorithm applied to Example 3. The common subspaces are two dimensional while the uncommon are three-dimensional for each system. We show the resulting embedding after imposing the orthogonality constraints in the latent space. Coloring is achieved as in to Fig. 3.

To produce the corresponding figures (Fig. 3), we use 54% of the data set for training, 36% for validation and 10% for testing. We terminate the first optimization step with training and validation losses of $1.8e-4$, $2.1e-4$ respectively, and the second optimization step with losses of $1.3e-3$, $7.3e-4$ respectively. The final test loss reported was $0.6e-3$ as well.

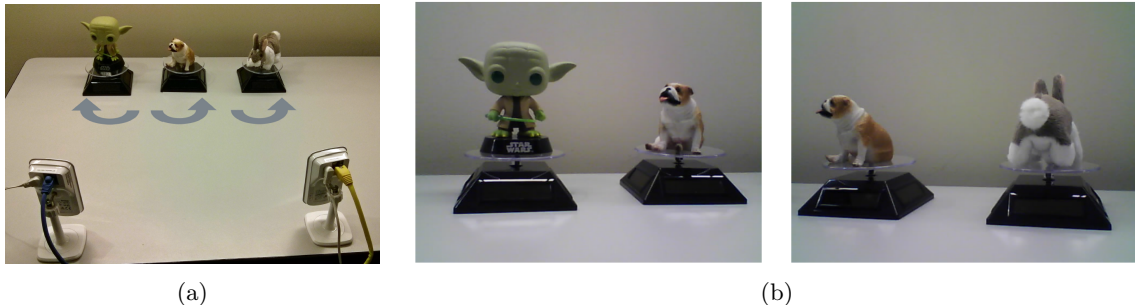


Figure 5: Bobblehead simulation setup presented in [3]. (We use the figures available in [15]). (a) gives a ‘bird-eye’ view of the setup, with the two cameras observing the bobblehead system; each bobblehead rotates independently with an unknown frequency. (b) shows each camera’s point of view at a specific point in time. The bulldog is ‘common’ between them but observed at different angles, while Yoda and the rabbit are ‘uncommon’.

Example 4 (Bobbleheads). Lastly, we consider the prototypical situation described in Example 1 where the roles of Alice, Bob, and Carol are played by rotating bobbleheads (Fig. 5 Yoda (\mathcal{U}), a Bulldog (\mathcal{C}), and a Rabbit (\mathcal{V})). These appeared in the original Alternating Diffusion work of [3]. We note that geometrically, the setting is identical to that of Example 2, with the difference being that we have to work with (higher-dimensional) images instead of the (lower embedding-dimensional) closed-curve trajectories considered previously.

Preprocessing: Our training set consists of 2500 pairs of RGB images in 320×250 pixels each, which are

converted to grayscale and compressed using their first 60 principal components. The PCA projection gives us a considerably smaller embedding dimension to work in computationally, but also ‘entangles’ the coordinates (pixels) of the three systems, with each PCA coordinate being a function of the pixels corresponding to *both* bobble-heads each sensor observes. One may in principle use random projections or a wavelet expansion instead and achieve a qualitatively similar result.

Training: We start by training a variant of the proposed architecture Appendix B.1, which we find to be more robust in identifying the common variable subspace. After identifying the common subspace, we train the original architecture (simply by switching the decoder inputs to what is depicted in Fig. 2) to also identify the uncommon systems. The final representations are portrayed in Fig. 6.

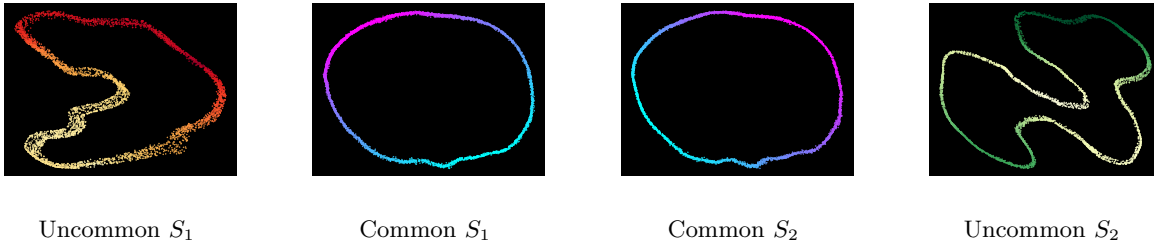


Figure 6: Latent embeddings produced by a single run of the optimization algorithm applied to Example 4. Each individual system corresponds to a limit cycle, as in Example 2, with points now representing images instead of oscillator trajectories. Here the ground-truth angles are not known; instead, the ‘common’ systems (middle-left, middle-right) are respectively colored by the two common coordinates approximated using the Alt-DMap algorithm of [2, 3]. The Uncommon systems are colored based on one of the two predictions of the Output-Informed Alt-DMap algorithm of [15].

Level Sets

Given an observation of camera 1, we know what the common features (the bulldog) in a simultaneous camera 2 observation will look like - but we do not know what the uncommon component of that observation will be. In fact, there exists an entire level set of camera 2 observations consistent with a particular camera 1 observation.

We further demonstrate the usefulness of our embeddings in producing such level sets. This is accomplished by generating ‘artificial’ images, exploiting the trained AE architecture (Fig. 7). We first embed an ‘original’ image in our computed, disentangled latent space, where the common and uncommon coordinates are represented by white ‘X’s. Then, after fixing either its (a) common coordinate or (b) uncommon coordinate, we randomly sample separate points in the alternate coordinate and feed the combination through the decoder. The reconstructed images are plausible observations, consistent with a fixed orientation for the common (resp. uncommon) bobble-head. Such a level set construction can be thought of as an extension of the Gappy-POD [16, 17], Gappy-Diffusion Maps [18] and Gappy-LOCA [19] computational workflows.

5 ‘Causal’ Learning

Throughout the examples of Section 4, we have assumed that each of the two sensors takes pictures (samples) *simultaneously*; this is natural in settings similar to Example 1.

However, it is possible to have a constant time difference Δt , or lag, between the observations of the two sensors, and *still* be able to achieve the objectives of Section 2. That is, a diffeomorphism φ as in Eqn. (6) may still exist. If, for each observation of Sensor 1 at time t , sensor 2 makes an observation at time $t + \Delta t$, and the dynamical system evolves smoothly and deterministically, the state (of the common system \mathcal{C}) at time $t + \Delta t$ is fully determined by integrating the state of the system at time t . This is the *flow map*:

$$\Phi_{\Delta t}^{\mathcal{C}} : (c_1, \dots, c_{d_c})(t) \mapsto (c_1, \dots, c_{d_c})(t + \Delta t).$$

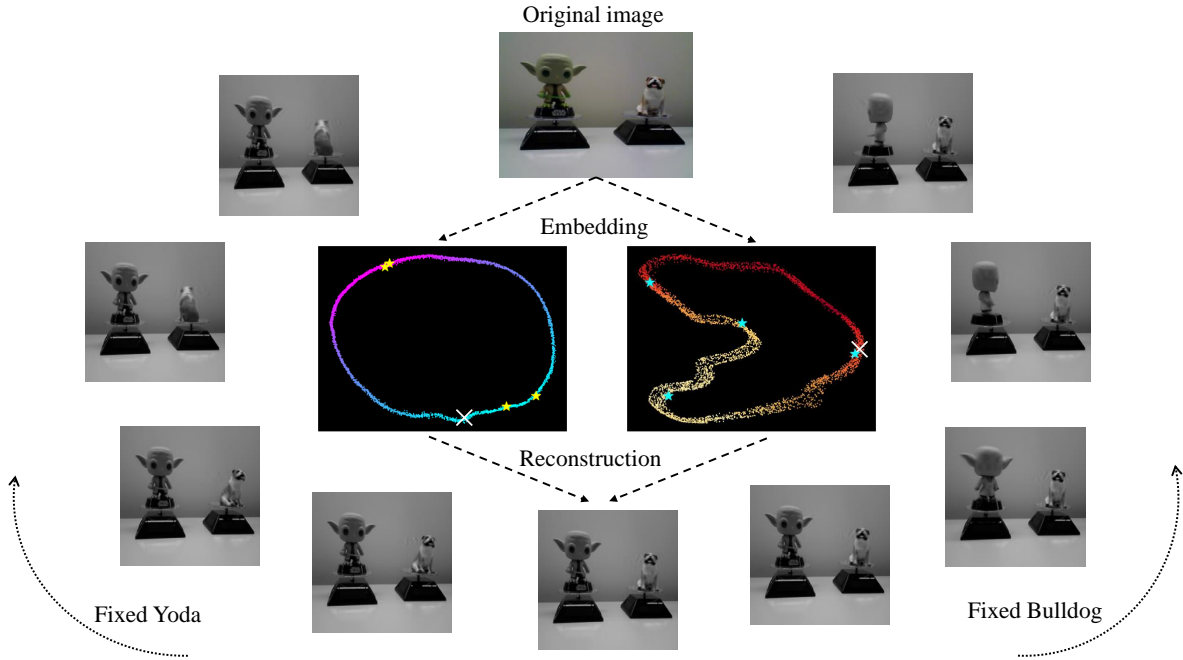


Figure 7: Images generated using the converged AE network. The larger white ‘X’ denote the embedding of the original image, which is reconstructed using the decoder approximation of its first 60 principal components. Then, we generate images consistent with either a fixed Bulldog (fixed common system, counter-clockwise) or even with a fixed Yoda (fixed uncommon system, clockwise) by fixing the corresponding common or uncommon coordinate and randomly varying over choices of points in the other coordinate (yellow \star for a varying bulldog and cyan \star for a varying yoda).

Of course, as Δt increases, numerical sensitivity issues arise when chaotic dynamics are involved.

To demonstrate the ability of the architecture to handle time-delayed data, we construct a simple example: We let \mathcal{C} be a common limit cycle, and \mathcal{U} be a Rössler attractor. The first sensor *only* observes the limit cycle at time t , while the second sensor observes the limit cycle at time $t + \Delta t$, as well as the uncommon system (here, $\Delta t = 200$ time units).

In this case, we do not scramble the data observed by the second sensor. Thus, observations have the form:

$$S_1 : (c_{1,t}, c_{2,t})$$

$$S_2 : (c_{1,t+\Delta t}, c_{2,t+\Delta t}, u_{1,t+\Delta t}, u_{2,t+\Delta t}, u_{3,t+\Delta t})$$

We train the architecture as previously proposed, to learn a common latent space and to disentangle the uncommon system that the second sensor observes. Then, encoding the observation of the second sensor (at time $t + \Delta t$) and using the decoder of the first sensor, we deduce (“post”dict) the state of the common dynamical system at time t . Mathematically this is described as:

$$\hat{\mathbf{c}}_t = \mathfrak{d}_1 \circ \pi_{1,2} \circ \mathfrak{e}_2(\mathbf{c}_{t+\Delta t}, \mathbf{u}_{t+\Delta t}) \quad (16)$$

where $\pi_{1,2}$ denotes a projection on the first two (here, the ‘common’) coordinates. In Fig. 8 we show that the predicted ($\hat{\mathbf{c}}_{t+\Delta t}$) and true state $\mathbf{c}_{t+\Delta t}$ of the system at time $t + \Delta t$ match, meaning that we can accurately integrate using the trained architecture, at least for this ‘simple’ example.

What this demonstrates is that this architecture can learn correlations between the present and future states of the dynamical system; That is, it can help establish a type of (correlational, Granger [20]) ‘causality’ among different asynchronous observations.

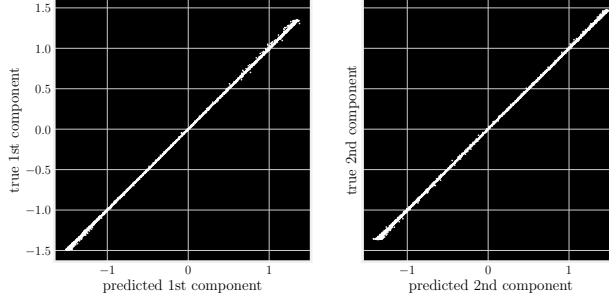


Figure 8: Relationship between the predicted ($\hat{\mathbf{c}}_t$) and true state (\mathbf{c}_t) of the common dynamical system at time t .

6 Discussion

In this work, we propose a structured autoencoder network architecture that, through training with a deliberately designed loss function, is capable of identifying ‘common’ information between two (or, in principle, more) heterogeneous data sets, and subsequently of *disentangling* and parametrizing information that is ‘uncommon’, i.e. unique to each data set. We demonstrate this task in a dynamical system setting, where we are able to ‘recover’ representations of underlying dynamical systems that are originally separated, but then ‘scrambled’ by a set of rotations. We show that the framework can be used when observations come in the form of high-dimensional images, as well as when there is a time-lag between them.

The implemented bi-level optimization algorithm demonstrates that the identification of the common subspace is, in some sense, a separate and simpler problem than the parametrization of the uncommon subspaces. It is natural to first parametrize the common subspace, in order to be able to subsequently define independence from it.

We note that the approach is completely unsupervised(!), given the key assumption of simultaneity across the data sets, and that the correct latent space dimensions are known. The architecture is still amenable to a semi-supervised objective, when the common or some uncommon system have already been previously identified (see e.g. [21]). These can be prescribed as supervised objectives in the algorithm, which then would seek to ‘complete the picture’ given this information (in analogy with the ‘gappy’ data context we referenced above). This also allows our method to be combined with other algorithmic routines (e.g. Alternating Diffusion) to compute the common subspace in cases where autoencoders might struggle compared to spectral methods (e.g. high extrinsic curvature of the embedded data). While we use fully connected layers in our architecture implementation, orthogonality constraints can similarly be used for alternative architectures such as convolutional autoencoders [22] to obtain disentangled latent representations.

Our definition of independence in this work is orthogonality of the subspaces on which the common and uncommon systems lie, in observation space. The algorithm attempts to find an embedding that makes these nonlinear subspaces mutually orthogonal. In that sense, it is purely geometric, in contrast to statistical disentanglement methods, such as nonlinear independent component analysis (NLICA) [10]. For example, we note that the uncommon system’s distribution need not be identical for every fixed point in the common system, it simply must lie in a (nearly) orthogonal subspace. Orthogonality is not affected by the boundaries of the observed data; conditional distributions are. Ultimately, depending on the problem at hand, the definition of independence matters. There may be problems where conformal and statistical independence coincide, though generically they do not. Such relations between geometric and statistical disentanglement warrant further study.

Regarding obstructions to conformal disentanglement, there are known results that limit the possibility of complete diagonalization of the metric tensor of a general manifold in dimensions 3 or 4 and above [23]. These do not directly apply to the present setting, since our metric is only block-diagonalized at particular points. Nevertheless, obstructions of a similar nature may hold. Fundamentally, the extent to which the data can be disentangled will be controlled by the structure of the Weyl tensor (generalized curvature) of

the manifold which they lie on. Thus, it is, in some sense, controlled by the regularity of the embedding maps (Φ_u^{-1}, Φ_v^{-1} in the notation of Section 2).

We state again that the setting easily generalizes to *multiple* data sets (beyond just two) that may share common information.

An important feature of this work is that (a) for unscrambled, ‘clean’ data, it allows us to learn a function between the different measurements of the common system by the two sensors: in effect, it constructs an *observer* of one sensor’s measurement of the common system from the other. More importantly, however, it allows us, given a measurement from the first sensor, to (b) create a sampling of all possible second sensor measurements consistent with it - a “level set” of what the second sensor may be observing at that time instance.

Interestingly, when one sensor measures a moment in time, and the second sensor measures the same variables at a later time, what is “common” between the two sensors allows us to identify the dynamical system itself, thus establishing a type of correlational causality across components of the sensor measurements

Data and Code Accessibility

The synthetic data sets used in the computational examples, along with accompanying code will become publically available upon publication. Regarding the bobble-head data set of Example 4 see the original publication [2].

Acknowledgements

The authors are grateful to Dr. D. Sroczynski for aiding in the synthetic data set generation, and to Professor R. Lederman for giving us access to the bobble-head image data set originally featured in [2]. The authors are thankful to Professors R. Lederman, R. Talmon, and R. Coifman and for helpful discussions and suggestions regarding this project. EDK was funded by the Luxembourg National Research Fund (FNR), grant reference 16758846. The work of YGK was partially supported by an AFOSR MURI (Dr. F. Fahroo);

References

- [1] B. Ekeroth and R. R. Coifman, “Perspective differentiation with diffusion geometry,” *ProQuest Dissertations and Theses, Yale University*, 2023.
- [2] R. R. Lederman and R. Talmon, “Common manifold learning using alternating-diffusion,” *submitted, Tech. Report YALEUIDCSITR1497*, 2014.
- [3] R. R. Lederman and R. Talmon, “Learning the geometry of common latent variables using alternating-diffusion,” *Applied and Computational Harmonic Analysis*, vol. 44, no. 3, pp. 509–536, 2018.
- [4] R. R. Coifman and S. Lafon, “Diffusion maps,” *Applied and Computational Harmonic Analysis*, vol. 21, no. 1, pp. 5–30, 2006. Special Issue: Diffusion Maps and Wavelets.
- [5] A. Holiday, M. Kooshkbaghi, J. M. Bello-Rivas, C. William Gear, A. Zagaris, and I. G. Kevrekidis, “Manifold learning for parameter reduction,” *Journal of Computational Physics*, vol. 392, pp. 419–431, 2019.
- [6] S. S. Lafon, *Diffusion maps and geometric harmonics*. Yale University, 2004.
- [7] N. Evangelou, N. J. Wichrowski, G. A. Kevrekidis, F. Dietrich, M. Kooshkbaghi, S. McFann, and I. G. Kevrekidis, “On the parameter combinations that matter and on those that do not: data-driven studies of parameter (non)identifiability,” *PNAS Nexus*, vol. 1, 09 2022. pgac154.
- [8] R. R. Coifman, N. F. Marshall, and S. Steinerberger, “A common variable minimax theorem for graphs,” *Foundations of Computational Mathematics*, vol. 23, no. 2, pp. 493–517, 2023.
- [9] W. K. Härdle, L. Simar, W. K. Härdle, and L. Simar, “Canonical correlation analysis,” *Applied multivariate statistical analysis*, pp. 443–454, 2015.
- [10] A. Hyvärinen and P. Pajunen, “Nonlinear independent component analysis: Existence and uniqueness results,” *Neural networks*, vol. 12, no. 3, pp. 429–439, 1999.
- [11] M. Cherti, R. Beaumont, R. Wightman, M. Wortsman, G. Ilharco, C. Gordon, C. Schuhmann, L. Schmidt, and J. Jitsev, “Reproducible scaling laws for contrastive language-image learning,” in *Proceedings of the IEEE/CVF Conference on Computer Vision and Pattern Recognition*, pp. 2818–2829, 2023.
- [12] L. Noakes, “The takens embedding theorem,” *International Journal of Bifurcation and Chaos*, vol. 1, no. 04, pp. 867–872, 1991.
- [13] H. Whitney, “Collected papers, volume ii,(james eells, domingo toledo, eds.),” 1992.
- [14] I. Higgins, L. Matthey, A. Pal, C. P. Burgess, X. Glorot, M. M. Botvinick, S. Mohamed, and A. Lerchner, “beta-vae: Learning basic visual concepts with a constrained variational framework,” *ICLR (Poster)*, vol. 3, 2017.
- [15] D. W. Sroczynski, F. Dietrich, E. D. Koronaki, R. Talmon, R. R. Coifman, E. Bolt, and I. G. Kevrekidis, “On learning what to learn: heterogeneous observations of dynamics and establishing (possibly causal) relations among them,” 2024.
- [16] E. D. Koronaki, N. Evangelou, Y. M. Psarellis, A. G. Boudouvis, and I. G. Kevrekidis, “From partial data to out-of-sample parameter and observation estimation with diffusion maps and geometric harmonics,” *Computers & Chemical Engineering*, vol. 178, p. 108357, 2023.
- [17] P. Papavasileiou, E. D. Koronaki, G. Pozzetti, M. Kathrein, C. Czettel, A. G. Boudouvis, and S. P. Bordas, “Equation-based and data-driven modeling strategies for industrial coating processes,” *Computers in Industry*, vol. 149, p. 103938, 2023.
- [18] C. P. Martin-Linares, Y. M. Psarellis, G. Karapetsas, E. D. Koronaki, and I. G. Kevrekidis, “Physics-agnostic and physics-infused machine learning for thin films flows: modelling, and predictions from small data,” *Journal of Fluid Mechanics*, vol. 975, p. A41, 2023.

- [19] E. Peterfreund, I. Burak, O. Lindenbaum, J. Gimlett, F. Dietrich, R. R. Coifman, and I. G. Kevrekidis, “Gappy local conformal auto-encoders for heterogeneous data fusion: in praise of rigidity,” *arXiv preprint arXiv:2312.13155*, 2023.
- [20] C. W. Granger, “Investigating causal relations by econometric models and cross-spectral methods,” *Econometrica: journal of the Econometric Society*, pp. 424–438, 1969.
- [21] G. Mishne, U. Shaham, A. Cloninger, and I. Cohen, “Diffusion nets,” *Applied and Computational Harmonic Analysis*, vol. 47, no. 2, pp. 259–285, 2019.
- [22] J. Masci, U. Meier, D. Cireşan, and J. Schmidhuber, “Stacked convolutional auto-encoders for hierarchical feature extraction,” in *Artificial Neural Networks and Machine Learning–ICANN 2011: 21st International Conference on Artificial Neural Networks, Espoo, Finland, June 14–17, 2011, Proceedings, Part I 21*, pp. 52–59, Springer, 2011.
- [23] D. M. DeTurck and D. Yang, “Existence of elastic deformations with prescribed principal strains and triply orthogonal systems,” *Duke mathematical journal*, vol. 51, no. 2, pp. 243–260, 1984.
- [24] A. Paszke, S. Gross, F. Massa, A. Lerer, J. Bradbury, G. Chanan, T. Killeen, Z. Lin, N. Gimeshein, L. Antiga, A. Desmaison, A. Kopf, E. Yang, Z. DeVito, M. Raison, A. Tejani, S. Chilamkurthy, B. Steiner, L. Fang, J. Bai, and S. Chintala, “Pytorch: An imperative style, high-performance deep learning library,” in *Advances in Neural Information Processing Systems 32*, pp. 8024–8035, Curran Associates, Inc., 2019.
- [25] D. P. Kingma and J. Ba, “Adam: A method for stochastic optimization,” *arXiv preprint arXiv:1412.6980*, 2014.

A Data and Network Architectures

A.1 Data Generation

Example 2 The data consists of samples of trajectories of three harmonic oscillations. The dynamics, i.e. the angle as a function of time $\theta(t)$ have the form:

$$\theta_i(t) = 2\pi\omega_i t$$

where the common and uncommon systems are characterized by

$$\mathcal{U} : \omega_1 = \frac{\pi}{2}, \quad \mathcal{V} : \omega_2 = \frac{\pi}{2\sqrt{2}}, \quad \mathcal{C} : \omega_3 = \frac{1}{\sqrt{2}}$$

Note that the ratios between each system’s frequencies are irrational, so as to avoid resonances. We sample a total of 3000 temporally equidistant points for each system. We ‘scramble’ the data using an invertible linear transformation, such that individual coordinates do not correspond to a single particular system for each sensor.

Example 3 The data consists of samples of trajectories for the following:

\mathcal{U} is sampled from a Rössler attractor:

$$\begin{aligned} \dot{x} &= -y - z \\ \dot{y} &= x + \alpha y \\ \dot{z} &= b + z(x - c) \end{aligned} \tag{17}$$

with $\alpha = b = 0.2$ and $c = 5.7$.

\mathcal{V} is sampled from a Lorenz attractor:

$$\begin{aligned} \dot{x} &= \sigma(y - x) \\ \dot{y} &= x(\rho - z) - y \\ \dot{z} &= xy - \beta z \end{aligned} \tag{18}$$

with $\sigma = 10$, $\beta = 8/3$, $\rho = 28$.

\mathcal{C} is sampled from a nonlinear limit cycle:

$$\begin{aligned} \dot{x} &= \alpha_1(1 - x - y) - \gamma_1 x - xy(1 - x - y)^2 \\ \dot{y} &= \alpha_2(1 - x - y) - \gamma_2 y - xy(1 - x - y)^2 \end{aligned} \tag{19}$$

with $\alpha_1 = 0.016$, $\gamma_1 = 0.001$, $\alpha_2 = 0.0278$, $\gamma_2 = 0.002$.

We sample a total of 3000 temporally equidistant points for the data set, using accurate numerical simulation. We ‘scramble’ the data using an invertible linear transformation, such that individual coordinates do not correspond to a single particular system for each sensor.

Example 4 The original data consists of colored RGB images of 320×240 pixels. There are 8100 images for each sensor (16200 total). Each bobble-head rotates circularly in one direction with an unknown frequency, while the frame rate is also unknown.

We randomly select 2500 pairs of snapshots as a training set, 700 as a validation set, and 1000 as a test set before optimization. These images are converted to gray-scale (single value per pixel), and compressed into square images with 240×240 pixels. Subsequently, they are projected onto their first 60 principal components, which are what the autoencoder architecture trains on. The principal components are computed per sensor, on the full set of 4200 randomly selected images.

Section 5 The data consists of samples of trajectories for dynamical systems. \mathcal{C} is a common limit cycle (as in Example 2) which sensor 1 observes at time t , and sensor 2 observes at time $t + \Delta t$, where $\Delta t = 200$.

The uncommon system \mathcal{U} observed by the second sensor is a Rössler attractor (as in Example 3). Note that sensor 1 does not observe any other system in this example.

We collect 2800 samples in time (for each system), and use a train/validation/test split of 54%, 36%, 10% respectively. The train and validation errors after the first optimization step are $1.2e-4$ and $1.5e-4$, for the run used to produce Fig. 8.

	min	max
Example 2	-2.20	2.20
Example 3	-3.66	7.73
Example 4	-8.02	10.83
Section 5	-2.08	8.11

Table 1: Minimum and maximum values of data both sensors after pre-processing, used to train the autoencoder weights.

We include nominal ranges of the data for each example after pre-processing in Table 1. These were used to train the autoencoder architecture in each case.

A.2 Architecture Details

Our neural networks are implemented in Python using PyTorch [24].

Example 2 All encoders and decoders consist of 7 fully connected linear layers the first 5 of which are composed with a tanh activation function. Each encoder layer has a width of 10 nodes and each decoder has a width of 20. Each encoder $\mathbf{e}_u^c, \mathbf{e}_v^c, \mathbf{e}_1^u, \mathbf{e}_2^u$ maps into two-dimensional latent subspaces, while decoder $\mathfrak{d}_1, \mathfrak{d}_2$ map the corresponding 4-dimensional latent spaces back into a Euclidean space of the same dimension (\mathbb{R}^4).

Example 3 All encoders and decoders consist of 7 fully connected linear layers the first 5 of which are composed with a tanh activation function. Each layer has a width of 30. Each common encoder $\mathbf{e}_u^c, \mathbf{e}_v^c$ maps to a two-dimensional common latent subspace, and each uncommon encoder $\mathbf{e}_u^c, \mathbf{e}_v^c$ maps to separate three-dimensional uncommon latent subspaces. Each decoder $\mathfrak{d}_1, \mathfrak{d}_2$ map the corresponding latent spaces back into a Euclidean space of the same dimension (\mathbb{R}^5). A sketch with the corresponding dimensions can be found in Fig. 2.

Example 4 All encoders consist of 7 fully connected linear layers the first 5 of which are composed with the tanh activation function. Each layer has width 40. Each encoder $\mathbf{e}_u^c, \mathbf{e}_v^c, \mathbf{e}_1^u, \mathbf{e}_2^u$ maps into two-dimensional latent subspaces. Each decoder $\mathfrak{d}_1, \mathfrak{d}_2$ has the same fully-connected structure as the encoder networks with a width of 80 nodes within each layer. They map the corresponding 4-dimensional latent spaces back into a Euclidean space \mathbb{R}^{60} , the truncated principal component representation of the images.

Section 5

B Optimization Algorithm

Algorithm 1 presents a more detailed sketch of the optimization scheme proposed in Section 3.2. In practice, we use Adam [25] instead of (Stochastic) Gradient Descent. We also note that we partition given data sets into train (used by the algorithm to evaluate and train on) validation (used by the algorithm during training to check performance on ‘unseen’ data) and test (only used after successful convergence to evaluate the performance of the algorithm) sets. This is common practice in network training and serves to avoid overfitting, but not represented in Algorithm 1 for the sake of clarity. The respective errors in each computational example are reported in Section 4.

In Algorithm 1, index i iterates over the samples of the data set, while indices j, k, l iterate over the dimensions (n_c, n_u, n_v) of the common and uncommon subspaces respectively.

Algorithm 1: CAE - Common Orthogonal Latent Decomposition

Data: Data sets (S_2, S_1)

Parameters: initialized CAE architecture and weights ($\mathbf{e}_1^c, \mathbf{e}_1^u, \mathbf{e}_2^c, \mathbf{e}_2^u, \mathbf{d}_1, \mathbf{d}_2$). Learning rate η , error tolerances ϵ_1, ϵ_2 are initialized to be small positive constants

Result: ‘Orthogonally disentangled’ common - uncommon latent representation of data

1st Level - Common subspace identification

while $\mathcal{L}_{CAE} \geq \epsilon_1$ **do**

// encoding and decoding forward pass

$$\{(\hat{\mathbf{u}}_i, \hat{\mathbf{c}}_{ui})\}_{i=1}^N = \{(\mathbf{e}_1^c(\mathbf{s}_{ui}), \mathbf{e}_1^u(\mathbf{s}_{ui}))\}_{i=1}^N \quad (20)$$

$$\{(\hat{\mathbf{v}}_i, \hat{\mathbf{c}}_{vi})\}_{i=1}^N = \{(\mathbf{e}_2^c(\mathbf{s}_{vi}), \mathbf{e}_2^u(\mathbf{s}_{vi}))\}_{i=1}^N \quad (21)$$

$$\{\hat{\mathbf{s}}_{ui}\}_{i=1}^N = \{\mathbf{d}_1(\hat{\mathbf{u}}_i, \hat{\mathbf{c}}_{ui})\}_{i=1}^N \quad (22)$$

$$\{\hat{\mathbf{s}}_{vi}\}_{i=1}^N = \{\mathbf{d}_2(\hat{\mathbf{v}}_i, \hat{\mathbf{c}}_{vi})\}_{i=1}^N \quad (23)$$

// compute reconstruction loss and common subspace loss

$$\mathcal{L}_{CAE} = \underbrace{\frac{1}{N} \sum_{i=1}^N \|\mathbf{s}_{ui} - \hat{\mathbf{s}}_{ui}\|_2^2 + \|\mathbf{s}_{vi} - \hat{\mathbf{s}}_{vi}\|_2^2}_{\text{Reconstruction}} + \underbrace{\frac{1}{N} \sum_{i=1}^N \|\hat{\mathbf{c}}_{ui} - \hat{\mathbf{c}}_{vi}\|_2^2}_{\text{Common Matching}} \quad (24)$$

// perform backward pass

$$w_{\mathbf{e}_1^u} - = \eta \nabla_{w_{\mathbf{e}_1^u}} \mathcal{L}_{CAE}, \quad w_{\mathbf{e}_1^c} - = \eta \nabla_{w_{\mathbf{e}_1^c}} \mathcal{L}_{CAE} \quad (25)$$

$$w_{\mathbf{e}_2^u} - = \eta \nabla_{w_{\mathbf{e}_2^u}} \mathcal{L}_{CAE}, \quad w_{\mathbf{e}_2^c} - = \eta \nabla_{w_{\mathbf{e}_2^c}} \mathcal{L}_{CAE} \quad (26)$$

$$w_{\mathbf{d}_1} - = \eta \nabla_{w_{\mathbf{d}_1}} \mathcal{L}_{CAE}, \quad w_{\mathbf{d}_2} - = \eta \nabla_{w_{\mathbf{d}_2}} \mathcal{L}_{CAE} \quad (27)$$

2nd Level - Uncommon subspace identification

while $\mathcal{L}_{CAE} \geq \epsilon_2$ **do**

encoding and decoding forward pass (same as in previous level)

// compute reconstruction and orthogonality loss

$$\mathcal{L}_{CAE} = \underbrace{\frac{1}{N} \sum_{i=1}^N \|\mathbf{s}_{ui} - \hat{\mathbf{s}}_{ui}\|_2^2 + \|\mathbf{s}_{vi} - \hat{\mathbf{s}}_{vi}\|_2^2}_{\text{Reconstruction}} + \underbrace{\frac{1}{N} \sum_{i=1}^N \sum_{j,k} \left\| \left\langle \nabla(\hat{\mathbf{c}}_{ui})_j, \nabla(\hat{\mathbf{u}}_i)_k \right\rangle \right\|_2^2 + \frac{1}{N} \sum_{i=1}^N \sum_{j,l} \left\| \left\langle \nabla(\hat{\mathbf{c}}_{vi})_j, \nabla(\hat{\mathbf{v}}_i)_l \right\rangle \right\|_2^2}_{\text{Common-Uncommon Orthogonality}} \quad (28)$$

// perform backward pass

$$w_{\mathbf{e}_1^u} - = \eta \nabla_{w_{\mathbf{e}_1^u}} \mathcal{L}_{CAE}, \quad w_{\mathbf{e}_2^u} - = \eta \nabla_{w_{\mathbf{e}_2^u}} \mathcal{L}_{CAE} \quad (29)$$

$$w_{\mathbf{d}_1} - = \eta \nabla_{w_{\mathbf{d}_1}} \mathcal{L}_{CAE}, \quad w_{\mathbf{d}_2} - = \eta \nabla_{w_{\mathbf{d}_2}} \mathcal{L}_{CAE} \quad (30)$$

B.1 Alternative Architectures

In the original architecture, we minimize the ‘common’ constraint $\mathcal{L}_{\text{common}}$ to bias the network towards finding the desired latent representation for the common variables. It is known, however, that minimizing multiple objectives in a loss function using gradient-descent-type algorithms can be difficult when the proper weighting of each term is unknown.

While the proposed implementation and algorithm in Section 3 is sufficient for the dynamical system computational examples, we observed this process not to be as stable in the case of Example 4, where the ambient dimension was significantly larger. In particular, minimizing $\mathcal{L}_{\text{common}}$ in this case resulted in the AE converging to ‘noise’ instead of any structured latent representation of the common variable. Reconstructions of the images featured an ‘averaged’ image for the bulldog, over its entire circular trajectory.

To remedy this issue, we propose the ‘Twisted’ variant of the architecture represented in Fig. 9. There, we ‘force’ the decoder for each sensor to view information from the encodings of both sensors. The only information from the first sensor relevant to the second one is, of course, related to the common variables, and *vice versa*. This architecture is capable of identifying the common submanifold (up to diffeomorphism) without minimizing an additional constraint.

We empirically found this architecture to be more robust to this convergence issue during training, and used it to produce the results in Example 4. After identifying the common submanifold, the inputs to the decoders can be switched to the original configuration of Fig. 2 before disentangling via the second step of Algorithm 1.

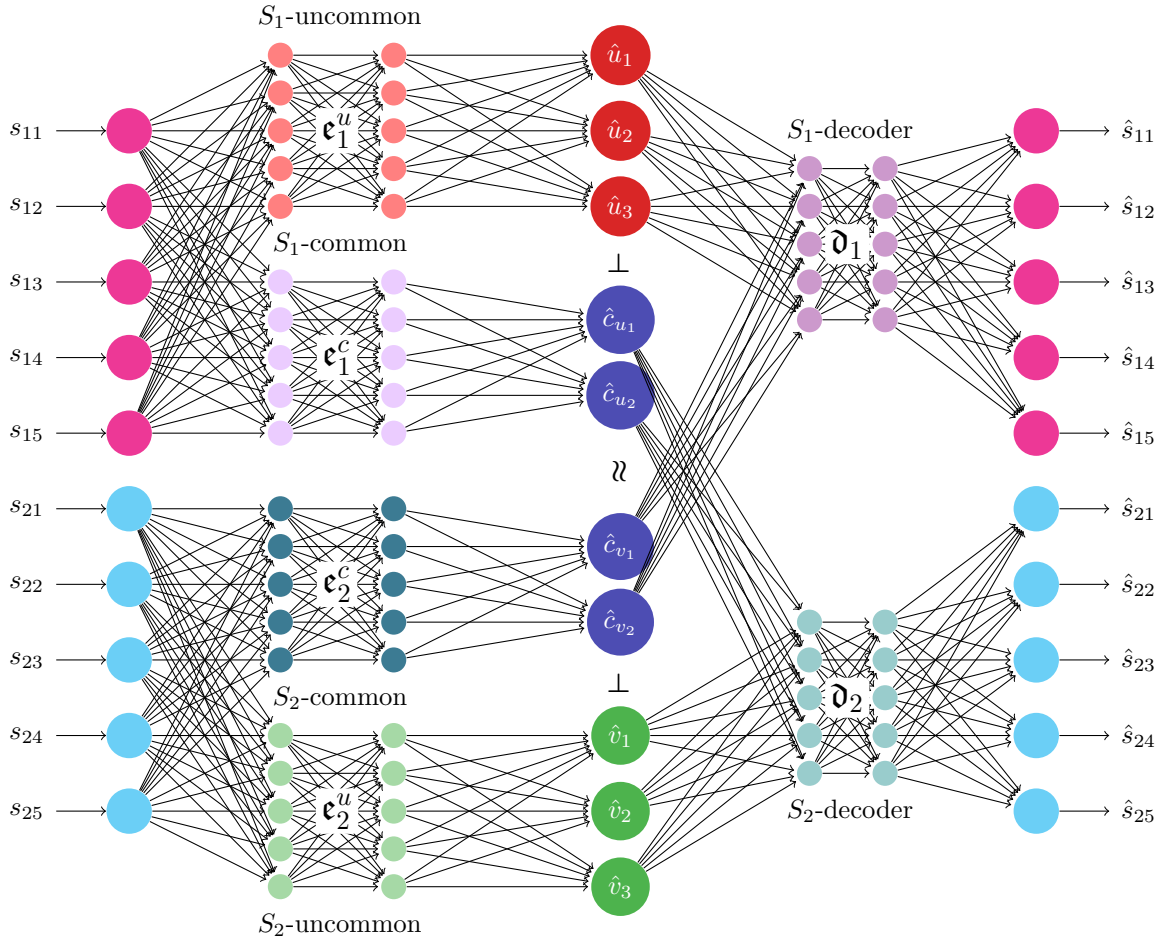


Figure 9: The ‘Twisted’ architecture is a variant of the original proposed architecture, where we bias the network to find a good common latent space by asking the reconstruction of each sensor to be influenced by the input to both sensors. This is achieved by changing the input to each decoder to use the ‘common’ information from the *other* sensor’s encoder.